Experimental validation of a coupled acoustic fluid-poroelastic-plate model with frontal and lateral source excitations

X.Sagartzazu*, L.M. Hervella-Nieto†, and A. Prieto‡

Abstract

This work deals with a coupled acoustic problem involving a compressible fluid and a poroelastic material contained in a cavity whose walls are all rigid except for the top, where a flexible plate is placed. The fluid is described utilizing its acoustic pressure, whereas, for the plate, the Naghdi model is used. The mechanical behaviour of the absorbing layer attached to the plate is described by using a Biot-Allard model, where the governing equations are written in the displacement-based formulation. A comprehensive three-dimensional analysis is performed, comparing numerical and experimental results and showing the advantages of using the Biot-Allard poroelastic model over other fluid-equivalent formulations, such as the Allard-Champoux model.

KEYWORDS: Fluid-poroelastic-plate coupling, Naghdi plate, Biot-Allard model, finite element method.

1 Introduction

The use of poroelastic materials is widespread across various industries. For instance, they are commonly employed in thermal applications [1], quasi-ceramic fibres used in burner designs [2], as well as veils, compression pads, and thermal barriers found in battery packs for electric vehicles [3]. In the realm of acoustic engineering, porous materials are often associated with passive noise control, which is of particular importance in sectors such as transportation and mobility ([4, 5]), consumer goods ([6, 7]), and the enhancement of acoustics within noisy rooms [8]. To effectively use poroelastic materials in these industrial applications, it is essential to understand the impact of introducing these materials on the mechanical system under consideration and to accurately identify their intrinsic properties, including flow resistivity and structural stiffness.

Therefore, with regard to vibroacoustic comfort, precise modelling of absorbing materials is essential for the development of passenger compartment designs. In classical literature, the mathematical modelling of these absorbing materials has been extensively detailed. Comprehensive reviews on the physical properties of such materials, methods for their measurement, various mathematical models, as well as their applications to different porous materials, can be found in sources such as [9, 10].

These references present three different approaches to modelling porous materials. The first approach involves experimental impedance measurements, which are detailed in sources such as

*Ikerlan Technological Research Center; P^o J.M. Arizmendiarreta, 20500 Arrasate-Mondragón, Gipuzkoa, Spain. E-mail: xsagartzazu@ikerlan.es

†CITIC. Universidade da Coruña, 15071, A Coruña, Spain. E-mail: luis.hervella@udc.es

‡CITMAga, Universidade da Coruña, 15071, A Coruña, Spain. E-mail: andres.prieto@udc.es

[11, 12]. The second approach treats the porous medium as a fluid-equivalent model with specific dissipative properties, as can be seen in [13–15]. Finally, the third approach involves modelling the material as an elastic medium comprising two media, with a structural stiffness associated with the solid phase and a fluid stiffness to account for fluid flow interaction. This approach is shown in works such as [16–18], all of which are based on Biot theory [19]. The most recent Biot-Allard model [9] includes the dissipative behaviour of poroelastic materials by introducing frequency-dependent damping expressions in the inertial and stress terms of the classical Biot model.

Further advances in the characterization of complex absorbing materials have been developed recently. For instance, Bravo and Maury [20] determined the key constitutive parameters that primarily influence the axial attenuation or normal absorption for rigidly-backed fibrous anisotropic materials in contact with a uniform mean flow. These parameters include fibre orientation and the degree of anisotropy. The absorption and attenuation properties of fibres with varying radii, randomly distributed in planes parallel to the surface, were modelled using Multiple Scattering Theory. Meanwhile, [21] analyzed the microstructure of sound-absorbing porous media with a rigid frame, taking into account the periodic geometry and using direct multi-scale computations as well as hybrid multi-scale calculations based on numerically determined transport parameters of porous materials. A similar approach was also used in [22] to derive new poroelastic Biot-like models from a two-scale homogenization procedure. Recently, other unphysical models that apply artificial intelligence methods, such as neural networks [23], have also emerged as data-driven modelling approaches.

In the process of selecting a method for modelling absorbing materials, it is essential to carefully consider the assumptions underlying each method and their respective ranges of validity. Reliable results in any numerical simulation also require experimental characterization of the material's mechanical properties, including its elastic stiffness, as well as the frequency range of interest and whether the vibrations are structural-borne or airborne in origin. Furthermore, it is important to keep in mind that each modelling approach has a different computational cost and generates qualitatively different frequency responses based on the angle of acoustic excitation. For instance, responses may vary depending on whether the excitation is normal or oblique when it impinges on the absorbing material.

In [17], a three-dimensional finite element model was developed to predict sound transmission loss through multilayer systems comprising elastic, acoustic, and poroelastic media. The three-dimensional poroelastic medium was modelled using the Biot theory, while a fluid-equivalent model was used to simulate fluid cavity absorption. However, this model becomes inaccurate when the absorbent is bonded to the elastic plate as the stiffness and damping of the absorbing material increase. In the subsequent work [18], the authors addressed the computational efficiency of different algorithms. They employed a three-dimensional finite element approach to solving the vibroacoustic coupled problem numerically, modelling the poroelastic material using the Biot-Allard theory. To avoid the need to recompute large frequency-dependent finite element matrices at each frequency step, they transformed the discretized equations of motion into a more appropriate form that explicitly separated the solid and fluid degrees of freedom.

Atalla *et al.* proposed a novel mixed displacement-pressure formulation for modelling poroelastic materials in [24]. In this formulation, the pressure field accounts for the compressible effects in a poroelastic medium, while the displacement field describes its overall vibrational behaviour. Compared to the classical two-displacement formulation, this pressure-displacement formulation has a significant computational advantage in reducing the number of degrees of freedom in the finite element implementations. Later on, the authors presented a three-dimensional finite element method for designing macro-perforated porous materials using a non-homogeneous porous media model in [25] and the mixed pressure-displacement formulation to model the poroelastic material. The results demonstrated that the proposed approach could effectively predict the acoustic properties of the designed materials.

The present study focuses on a three-dimensional coupled problem involving a compressible fluid and a poroelastic material that is attached to an elastic plate. The Biot-Allard model describes the absorbing material's behaviour, while the elastic plate is modelled using the Naghdi model, which accounts for the transversal and in-plane structural displacements. The coupling between these three types of elements in the mechanical system increases the complexity of understanding the system's frequency response. Although a mixed pressure-displacement formulation could benefit the discretization of the poroelastic material, a displacement-displacement formulation is employed to achieve a natural coupling with respect to the degrees of freedom of the Naghdi plate displacements. In addition, an acoustic pressure-based model is used to describe the adiabatic compressional effects on the fluid cavity. The in-house finite element implementation has been validated using a simplified problem with a known analytical solution. Then the obtained numerical results were compared with experimental data from two different types of absorbing materials. Furthermore, the numerical frequency responses obtained with the Biot-Allard model and the fluid-equivalent Allard-Champoux model have also been analyzed when the acoustic source is placed in a frontal or lateral location with respect to the position of the absorbing poroelastic layer.

The structure of this paper is organized as follows. Section 2 presents the strong formulation of the problem. Section 3 introduces the variational formulation, and subsequently, it is discretized in Section 4 by presenting its matrix formulation. The numerical implementation of the proposed finite element code is validated in Section 5 by using a three-dimensional benchmark with plane-wave solutions, and it shows the expected order of convergence. In Section 6, numerical and experimental results highlight the differences between the fluid-equivalent and Biot-Allard models. Finally, the main conclusions of this numerical and experimental study are included in Section 7.

2 Porous-fluid-plate coupled model

Throughout this work, all the acoustic sources are assumed time-harmonic, with a time dependence $e^{-i\omega t}$, being ω the angular frequency. Consequently, the solution is also time-harmonic due to the linearity of the coupled problem considered throughout this manuscript. Hence, all the computations are implicitly assumed in the frequency domain. Two-dimensional cuts of the geometrical setting of the coupled problem are shown in Figure 1(a).

As usual for interior vibroacoustic problems (see [26], for example), exterior loads are neglected, and the compressible fluid in Ω_{F} is assumed to be homogeneous, inviscid, barotropic, and ideal. Then, it can be modelled by means of the Lagrangian fluctuation of the pressure, p_{F}, governed by the classical Helmholtz equation,

$$-\frac{1}{\rho_{\mathrm{F}}\omega^2}\Delta p_{\mathrm{F}} - \frac{1}{\rho_{\mathrm{F}} c_{\mathrm{F}}^2} p_{\mathrm{F}} = g \qquad \text{in } \Omega_{\mathrm{F}}, \tag{1}$$

where ρ_{F} and c_{F} stand for the fluid mass density and the sound speed within it, and g is the acoustic volumetric source in the fluid subdomain.

To describe the vibrations of the poroelastic material, the classical $(\mathbf{u}_{\mathrm{A}}^{\mathrm{F}}, \mathbf{u}_{\mathrm{A}}^{\mathrm{S}})$-displacement formulation of the Biot-Allard equations (see [9, 19]) has been used. The Biot-Allard equations consider two stress tensors that describe the internal loads resulting from the presence of fluid and solid phases within the poroelastic material. These stress tensors can be mathematically expressed

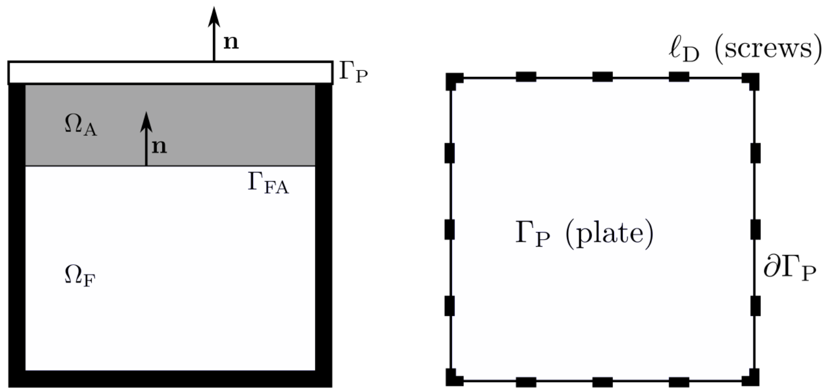

(a) A two-dimensional vertical cut of the computational domain

(b) Detail of the locations of the screws for fixing the plate

Figure 1: The computational domain is composed of the fluid, the poroelastic subdomains (highlighted in white and grey, respectively), and the plate on the top (left). The rigid walls are marked in black. The screw boundaries on the plate are highlighted with thick black thick segments (right).

as follows:

$$
\begin{aligned}
\boldsymbol{\sigma}_{\mathrm{A}}^{\mathrm{S}} &= (P_{\mathrm{A}} - 2N_{\mathrm{A}})(\operatorname{div} \mathbf{u}_{\mathrm{A}}^{\mathrm{S}})I + 2N_{\mathrm{A}}\boldsymbol{\epsilon}(\mathbf{u}_{\mathrm{A}}^{\mathrm{S}}) + Q_{\mathrm{A}}(\operatorname{div} \mathbf{u}_{\mathrm{A}}^{\mathrm{F}})I, \\
\boldsymbol{\sigma}_{\mathrm{A}}^{\mathrm{F}} &= R_{\mathrm{A}}(\operatorname{div} \mathbf{u}_{\mathrm{A}}^{\mathrm{F}})I + Q_{\mathrm{A}}(\operatorname{div} \mathbf{u}_{\mathrm{A}}^{\mathrm{S}})I,
\end{aligned}
$$

where $\boldsymbol{\epsilon}$ is the three-dimensional strain tensor defined by

$$
\epsilon_{ij}(\mathbf{u}) = \frac{1}{2}\left(\frac{\partial u_i}{\partial x_j} + \frac{\partial u_j}{\partial x_i}\right), \quad 1 \le i, j \le 3. \tag{2}
$$

The coefficients involved in the fluid and solid stress tensors can be expressed in terms of the elastic mechanical properties of the fluid and the solid frame of the poroelastic material as follows:

$$
\begin{aligned}
N_{\mathrm{A}} &= \frac{E_{\mathrm{A}}(1 + i\eta_{\mathrm{A}})}{2(1+\nu_{\mathrm{A}})}, \qquad P_{\mathrm{A}} = \frac{2N_{\mathrm{A}}(1+\nu_{\mathrm{A}})}{3(1-2\nu_{\mathrm{A}})} + \frac{4}{3}N_{\mathrm{A}} + \frac{(1-\phi)^2}{\phi}K(\omega), \\
Q_{\mathrm{A}} &= (1-\phi)K(\omega), \qquad R_{\mathrm{A}} = \phi K(\omega),
\end{aligned}
$$

where E_{A}, η_{A}, and ν_{A} denote the Youngs' modulus, the loss factor, and the Poisson coefficient of the elastic material of the solid frame of the poroelastic material, respectively. In contrast to the classical Biot model, where no dissipative effects are included in the stress tensor, the Biot-Allard model accounts for the viscous and thermal losses in the microstructure of the poroelastic material. In that manner, the frequency-dependent dynamic bulk modulus,

$$
K(\omega) = \gamma P_0 \left(\gamma - (\gamma - 1) \middle/ \left(1 + \frac{8\eta_{\mathrm{F}}}{i\Lambda'^2 \mathrm{Pr}\,\omega\rho_{\mathrm{F}}}\sqrt{\frac{1 + i\rho_{\mathrm{F}}\omega \mathrm{Pr}\,\Lambda'^2}{16\eta_{\mathrm{F}}}}\right)\right)^{-1},
$$

has been involved in the expression of the tensor coefficients. In the expression above, ρ_{F} and ρ_{S} denote the mass density of the saturated fluid and the solid skeleton of the porous material, respectively, and ϕ and Λ' are the porosity and the characteristic thermal length of the porous material. Additionally, the expression of $K(\omega)$ involves four saturated fluid-related parameters:

the atmospheric pressure, $P_0 = 101320$ Pa, and the adimensional Prandtl' number, $\mathrm{Pr} = 0.71$, the ratio for the specific heats $\gamma = 1.4$, and the dynamic fluid viscosity of the saturated fluid $\eta_{\mathrm{F}} = 1.81 \times 10^{-5}\,\mathrm{Pa\,s}$.

Considering the stiffness and the inertial terms, the Biot-Allard model in the absorbing subdomain, Ω_{A}, can be posed as

$$
\begin{aligned}
-\operatorname{div} \boldsymbol{\sigma}_{\mathrm{A}}^{\mathrm{F}} - \omega^2 \hat{\rho}_{22}(\omega)\mathbf{u}_{\mathrm{A}}^{\mathrm{F}} - \omega^2 \hat{\rho}_{12}(\omega)\mathbf{u}_{\mathrm{A}}^{\mathrm{S}} &= \mathbf{0} \qquad \text{in } \Omega_{\mathrm{A}}, \qquad (3)\\
-\operatorname{div} \boldsymbol{\sigma}_{\mathrm{A}}^{\mathrm{S}} - \omega^2 \hat{\rho}_{11}(\omega)\mathbf{u}_{\mathrm{A}}^{\mathrm{S}} - \omega^2 \hat{\rho}_{12}(\omega)\mathbf{u}_{\mathrm{A}}^{\mathrm{F}} &= \mathbf{0} \qquad \text{in } \Omega_{\mathrm{A}}. \qquad (4)
\end{aligned}
$$

The inertial terms in the Biot-Allard model involve $\hat{\rho}_{11}$ and $\hat{\rho}_{22}$, which represent, respectively, the mass densities of the fluid and solid frames in the porous medium, and $\hat{\rho}_{12}$ the inertial coupling between both phases. To model the dissipative effects of the poroelastic material, the Biot-Allard mass damping is included in the mass coefficients given by (see [9])

$$
\begin{aligned}
\hat{\rho}_{11}(\omega) &= \rho_{\mathrm{S}} - \hat{\rho}_{12}(\omega),\\
\hat{\rho}_{12}(\omega) &= -\phi\rho_{\mathrm{F}}(\alpha_\infty - 1) + ir\phi^2 \frac{G(\omega)}{\omega},\\
\hat{\rho}_{22}(\omega) &= \phi\rho_{\mathrm{F}} - \hat{\rho}_{12}(\omega),
\end{aligned}
$$

with $G(\omega) = \sqrt{1 + i4\alpha_\infty^2 \eta_{\mathrm{F}} \rho_{\mathrm{F}} \omega / (r\Lambda\phi)}$, being r the flow resistivity of the poroelastic material, α_∞ the tortuosity and Λ the characteristic viscous length of the poroelastic material.

Finally, the Naghdi model [27] has been used to model the elastic plate's behaviour, which takes into account the shear strain on the mid surface of the plate, Γ_{P}. This model is written by means of, by one side, the displacements of the mean surface of the plate, $\mathbf{u}_{\mathrm{P}} = \left(u_{\mathrm{P}}^1, u_{\mathrm{P}}^2, u_{\mathrm{P}}^3\right)$, decomposed into in-plane (membrane) displacements, $\mathbf{u}_{\mathrm{P}}^{\mathrm{M}} = \left(u_{\mathrm{P}}^1, u_{\mathrm{P}}^2\right)$, and normal displacements, u_{P}^3, and, by the other side, the rotations of the fibers initially normal to the plate surface, $\boldsymbol{\beta}_{\mathrm{P}} = \left(\beta_{\mathrm{P}}^1, \beta_{\mathrm{P}}^2\right)$. Then, the model splits into two uncoupled systems of equations: First, the Reissner-Mindlin equations for the transverse displacements:

$$
\begin{aligned}
-\frac{t^3 E_{\mathrm{P}}}{24\left(1-\nu_{\mathrm{P}}^2\right)} &\left[(1-\nu_{\mathrm{P}})\,\Delta\boldsymbol{\beta}_{\mathrm{P}} + (1+\nu_{\mathrm{P}})\,\boldsymbol{\nabla}\operatorname{div}\boldsymbol{\beta}_{\mathrm{P}}\right]\\
&- \frac{k_{\mathrm{P}} t E_{\mathrm{P}}}{2\,(1+\nu_{\mathrm{P}})}\left[\boldsymbol{\nabla} u_{\mathrm{P}}^3 - \boldsymbol{\beta}_{\mathrm{P}}\right] - \omega^2 \frac{t^3 \rho_{\mathrm{P}}}{12}\boldsymbol{\beta}_{\mathrm{P}} = \mathbf{0} \qquad \text{on } \Gamma_{\mathrm{P}}, \qquad (5)\\
&- \frac{k_{\mathrm{P}} t E_{\mathrm{P}}}{2\,(1+\nu_{\mathrm{P}})}\left(\Delta u_{\mathrm{P}}^3 - \operatorname{div}\boldsymbol{\beta}_{\mathrm{P}}\right) - \omega^2 t\rho_{\mathrm{P}} u_{\mathrm{P}}^3 = g_{\mathrm{P}} \qquad \text{on } \Gamma_{\mathrm{P}}. \qquad (6)
\end{aligned}
$$

Here, t stands for the thickness of the plate, E_{P} is its Young modulus, ν_{P} the Poisson ratio, k_{P} a shear strain correction factor (which is usually fixed to $5/6$ for clamped plates), ρ_{P} is the mass density of the plate, and g_{P} is the structural load (pressure) exerted on the plate. Secondly, the two-dimensional linear elasticity equation accounts for the in-plane plate motion:

$$
-\frac{E_{\mathrm{P}} t}{12\left(1-\nu_{\mathrm{P}}^2\right)}\left[(1-\nu_{\mathrm{P}})\,\boldsymbol{\Delta}\mathbf{u}_{\mathrm{P}}^{\mathrm{M}} + (1+\nu_{\mathrm{P}})\,\boldsymbol{\nabla}\operatorname{div}\mathbf{u}_{\mathrm{P}}^{\mathrm{M}}\right] - \omega^2 t\rho_{\mathrm{P}}\mathbf{u}_{\mathrm{P}}^{\mathrm{M}} = \mathbf{0} \qquad \text{on } \Gamma_{\mathrm{P}}. \qquad (7)
$$

Regarding the coupling conditions between the different media, and the boundary conditions, kinematic and kinetic conditions must be imposed among the fluid, the poroelastic, and the plate:

(A) Coupling conditions on the fluid-poroelastic interface Γ_{FA}:

(A.1) The continuity of fluid and poroelastic loads is ensured by taking into account the balance of the loads in terms of the fluid and solid stress tensors in the poroelastic material as follows:

$$\boldsymbol{\sigma}_{\mathrm{A}}^{\mathrm{F}}\mathbf{n} = -\phi p_{\mathrm{F}}\mathbf{n}, \qquad \boldsymbol{\sigma}_{\mathrm{A}}^{\mathrm{S}}\mathbf{n} = -(1-\phi)p_{\mathrm{F}}\mathbf{n} \qquad \text{on } \Gamma_{\mathrm{FA}},$$

where ϕ is the porosity of the porous material.

(A.2) Equality of normal displacements (slipping condition):

$$\frac{1}{\rho_{\mathrm{F}}\omega^2}\frac{\partial p_{\mathrm{F}}}{\partial \mathbf{n}} = \left((1-\phi)\mathbf{u}_{\mathrm{A}}^{\mathrm{S}} + \phi\mathbf{u}_{\mathrm{A}}^{\mathrm{F}}\right)\cdot\mathbf{n} = \left(\mathbf{u}_{\mathrm{A}}^{\mathrm{S}} + \phi(\mathbf{u}_{\mathrm{A}}^{\mathrm{F}} - \mathbf{u}_{\mathrm{A}}^{\mathrm{S}})\right)\cdot\mathbf{n} \qquad \text{on } \Gamma_{\mathrm{FA}}.$$

(B) Coupling conditions at the poroelastic-plate interface Γ_{P}:

(B.1) Continuity of loads: $\left(\boldsymbol{\sigma}_{\mathrm{A}}^{\mathrm{F}} + \boldsymbol{\sigma}_{\mathrm{A}}^{\mathrm{S}}\right)\mathbf{n} = g_{\mathrm{P}}\mathbf{n}$ on Γ_{P}, where g_{P} is the load exerted on the plate (see the right-hand side in (6)).

(B.2) Equality of normal displacements between the plate and the fluid part of the absorbing medium (slipping condition) and equality of displacements between the plate and the solid part of the absorbing medium (no-slipping condition),

$$\mathbf{u}_{\mathrm{A}}^{\mathrm{F}}\cdot\mathbf{n} = \mathbf{u}_{\mathrm{P}}\cdot\mathbf{n} = u_{\mathrm{P}}^3, \qquad \mathbf{u}_{\mathrm{A}}^{\mathrm{S}} = \mathbf{u}_{\mathrm{P}} \qquad \text{on } \Gamma_{\mathrm{P}}.$$

(C) Boundary conditions on the outer boundaries of the computational domain:

(C.1) Null normal displacements on the walls of the fluid subdomain,

$$\frac{1}{\rho_{\mathrm{F}}\omega^2}\frac{\partial p_{\mathrm{F}}}{\partial \mathbf{n}} = 0 \qquad \text{on } \Gamma_{\mathrm{N}}\cap\partial\Omega_{\mathrm{F}}.$$

(C.2) Null normal displacements of the solid part and the fluid part on the walls of the absorbent subdomain, this is,

$$\mathbf{u}_{\mathrm{A}}^{\mathrm{S}}\cdot\mathbf{n} = \mathbf{0}, \qquad \mathbf{u}_{\mathrm{A}}^{\mathrm{F}}\cdot\mathbf{n} = \mathbf{0} \qquad \text{on } \Gamma_{\mathrm{D}}\cap\partial\Omega_{\mathrm{A}}.$$

(D) Boundary conditions for the plate:

(D.1) Null normal displacements of the mean surface of the plate in the locations of the screws and null rotations of the fibres that were initially normal to the plate surface in the same locations,

$$\mathbf{u}_{\mathrm{P}} = \mathbf{0}, \qquad \boldsymbol{\beta}_{\mathrm{P}} = \mathbf{0} \qquad \text{on } \ell_{\mathrm{D}}.$$

(D.2) Free conditions on the exterior boundary of the plate, outside the screws (see [28]),

$$\mathbf{n}\cdot\boldsymbol{C}(\boldsymbol{\beta}_{\mathrm{P}})\mathbf{n} = \mathbf{s}\cdot\boldsymbol{C}(\boldsymbol{\beta}_{\mathrm{P}})\mathbf{n} = 0, \qquad \frac{\partial u_{\mathrm{P}}^3}{\partial \mathbf{n}} = \boldsymbol{\beta}_{\mathrm{P}}\cdot\mathbf{n} \qquad \text{on } \partial\Gamma_{\mathrm{P}}\setminus\ell_{\mathrm{D}},$$

where $\boldsymbol{C}$ stands for the tensor associated with the linear elasticity in the plate, appearing in the first term of equation (5), and $\mathbf{s}$ denotes the unitary vector tangential to the plate boundary.

A detailed analysis of the importance to consider bolted boundary conditions versus clamped ones is described in [29], where the shear correction factor is assumed $k_{\mathrm{P}} = 5/6$.

3 Variational formulation

In order to apply a classical numerical Galerkin-type method (i.e., a finite element method), a variational formulation must be obtained from the coupled system (1)-(7) jointly with the coupling boundary conditions and boundary conditions, (A)-(D). For this purpose, an adequate functional space must be settled for the trial and the test functions of the weak problem associated with the coupled problem. Attending to the differential operators involved in the governing equations, the solution to the variational problem is sought in

$$\mathbf{V} = \Big\{ \left(q_{\mathrm{F}}, \mathbf{v}_{\mathrm{A}}^{\mathrm{F}}, \mathbf{v}_{\mathrm{A}}^{\mathrm{S}}, \mathbf{v}_{\mathrm{P}}, \boldsymbol{\eta}_{\mathrm{P}}\right) \in \mathrm{H}^1(\Omega_{\mathrm{F}}) \times \left(\mathrm{H}^1(\Omega_{\mathrm{A}})\right)^3 \times \left(\mathrm{H}^1(\Omega_{\mathrm{A}})\right)^3 \times \left(\mathrm{H}^1(\Gamma_{\mathrm{P}})\right)^3 \times \left(\mathrm{H}^1(\Gamma_{\mathrm{P}})\right)^2 : \\ \mathbf{v}_{\mathrm{A}}^{\mathrm{F}} \cdot \mathbf{n}\big|_{\Gamma_{\mathrm{P}}} = v_{\mathrm{P}}^3,\ \mathbf{v}_{\mathrm{A}}^{\mathrm{S}}\big|_{\Gamma_{\mathrm{P}}} = \mathbf{v}_{\mathrm{P}},\ \mathbf{v}_{\mathrm{A}}^{\mathrm{F}} \cdot \mathbf{n}\big|_{\partial\Omega_{\mathrm{A}}\cap\Gamma_{\mathrm{D}}} = \mathbf{v}_{\mathrm{A}}^{\mathrm{S}} \cdot \mathbf{n}\big|_{\partial\Omega_{\mathrm{A}}\cap\Gamma_{\mathrm{D}}} = \mathbf{0},\ \mathbf{v}_{\mathrm{P}}\big|_{\ell_{\mathrm{D}}} = \boldsymbol{\eta}_{\mathrm{P}}\big|_{\ell_{\mathrm{D}}} = \mathbf{0} \Big\}. \quad (8)$$

Once the governing equations (1)-(7) are multiplied by their respective test functions q_{F}, $\mathbf{v}_{\mathrm{A}}^{\mathrm{F}}$, $\mathbf{v}_{\mathrm{A}}^{\mathrm{S}}$, $\mathbf{v}_{\mathrm{P}}$, $\boldsymbol{\eta}_{\mathrm{P}}$, and after applying Green's formulae considering the corresponding coupling and boundary coupling conditions, the variational formulation of the problem can be written as follows (see [30] for further details): *Find* $\left(p_{\mathrm{F}}, \mathbf{u}_{\mathrm{A}}^{\mathrm{F}}, \mathbf{u}_{\mathrm{A}}^{\mathrm{S}}, \mathbf{u}_{\mathrm{P}}, \boldsymbol{\beta}_{\mathrm{P}}\right) \in \mathbf{V}$ *such that*

$$\begin{aligned}
&\int_{\Omega_{\mathrm{F}}} \frac{1}{\rho_{\mathrm{F}}\omega^2} \boldsymbol{\nabla} p_{\mathrm{F}} \cdot \boldsymbol{\nabla} q_{\mathrm{F}} \mathrm{d}\Omega - \int_{\Omega_{\mathrm{F}}} \frac{1}{\rho_{\mathrm{F}} c_{\mathrm{F}}^2} p_{\mathrm{F}} q_{\mathrm{F}} \mathrm{d}\Omega - \int_{\Gamma_{\mathrm{FA}}} \phi \left(\mathbf{u}_{\mathrm{A}}^{\mathrm{F}} \cdot \mathbf{n}\right) q_{\mathrm{F}} \mathrm{d}\Gamma - \int_{\Gamma_{\mathrm{FA}}} (1-\phi) \left(\mathbf{u}_{\mathrm{A}}^{\mathrm{S}} \cdot \mathbf{n}\right) q_{\mathrm{F}} \mathrm{d}\Gamma \\
&- \int_{\Gamma_{\mathrm{FA}}} \phi p_{\mathrm{F}} (\mathbf{v}_{\mathrm{A}}^{\mathrm{F}} \cdot \mathbf{n}) \mathrm{d}\Gamma + R_{\mathrm{A}} \int_{\Omega_{\mathrm{A}}} \operatorname{div} \mathbf{u}_{\mathrm{A}}^{\mathrm{F}} \operatorname{div} \mathbf{v}_{\mathrm{A}}^{\mathrm{F}} \mathrm{d}\Omega + Q_{\mathrm{A}} \int_{\Omega_{\mathrm{A}}} \operatorname{div} \mathbf{u}_{\mathrm{A}}^{\mathrm{S}} \operatorname{div} \mathbf{v}_{\mathrm{A}}^{\mathrm{F}} \mathrm{d}\Omega - \int_{\Omega_{\mathrm{A}}} \omega^2 \hat{\rho}_{22} \mathbf{u}_{\mathrm{A}}^{\mathrm{F}} \cdot \mathbf{v}_{\mathrm{A}}^{\mathrm{F}} \mathrm{d}\Omega \\
&- \int_{\Omega_{\mathrm{A}}} \omega^2 \hat{\rho}_{12} \mathbf{u}_{\mathrm{A}}^{\mathrm{S}} \cdot \mathbf{v}_{\mathrm{A}}^{\mathrm{F}} \mathrm{d}\Omega - \int_{\Gamma_{\mathrm{FA}}} (1-\phi) p_{\mathrm{F}} (\mathbf{v}_{\mathrm{A}}^{\mathrm{S}} \cdot \mathbf{n}) \mathrm{d}\Gamma + (P_{\mathrm{A}} - 2N_{\mathrm{A}}) \int_{\Omega_{\mathrm{A}}} \operatorname{div} \mathbf{u}_{\mathrm{A}}^{\mathrm{S}} \operatorname{div} \mathbf{v}_{\mathrm{A}}^{\mathrm{S}} \mathrm{d}\Omega \\
&+ 2N_{\mathrm{A}} \int_{\Omega_{\mathrm{A}}} \boldsymbol{\epsilon}\left(\mathbf{u}_{\mathrm{A}}^{\mathrm{S}}\right) : \boldsymbol{\epsilon}\left(\mathbf{v}_{\mathrm{A}}^{\mathrm{S}}\right) \mathrm{d}\Omega + Q_{\mathrm{A}} \int_{\Omega_{\mathrm{A}}} \operatorname{div} \mathbf{u}_{\mathrm{A}}^{\mathrm{F}} \operatorname{div} \mathbf{v}_{\mathrm{A}}^{\mathrm{S}} \mathrm{d}\Omega - \int_{\Omega_{\mathrm{A}}} \omega^2 \hat{\rho}_{11} \mathbf{u}_{\mathrm{A}}^{\mathrm{S}} \cdot \mathbf{v}_{\mathrm{A}}^{\mathrm{S}} \mathrm{d}\Omega - \int_{\Omega_{\mathrm{A}}} \omega^2 \hat{\rho}_{12} \mathbf{u}_{\mathrm{A}}^{\mathrm{F}} \cdot \mathbf{v}_{\mathrm{A}}^{\mathrm{S}} \mathrm{d}\Omega \\
&+ \frac{t^3}{12} \int_{\Gamma_{\mathrm{P}}} \boldsymbol{\epsilon}_{\mathrm{P}}(\boldsymbol{\beta}_{\mathrm{P}}) : \boldsymbol{\epsilon}_{\mathrm{P}}(\boldsymbol{\eta}_{\mathrm{P}}) \mathrm{d}\Gamma + t \int_{\Gamma_{\mathrm{P}}} \boldsymbol{\epsilon}_{\mathrm{P}}(\mathbf{u}_{\mathrm{P}}^{\mathrm{M}}) : \boldsymbol{\epsilon}_{\mathrm{P}}(\mathbf{v}_{\mathrm{P}}^{\mathrm{M}}) \mathrm{d}\Gamma + k_{\mathrm{P}} t \int_{\Gamma_{\mathrm{P}}} \left(\boldsymbol{\nabla} u_{\mathrm{P}}^3 - \boldsymbol{\beta}_{\mathrm{P}}\right) \cdot \left(\boldsymbol{\nabla} v_{\mathrm{P}}^3 - \boldsymbol{\eta}_{\mathrm{P}}\right) \mathrm{d}\Gamma \\
&- \int_{\Gamma_{\mathrm{P}}} \omega^2 \rho_{\mathrm{P}} \mathbf{u}_{\mathrm{P}} \mathbf{v}_{\mathrm{P}} \mathrm{d}\Gamma - \omega^2 \frac{t^3}{12} \int_{\Gamma_{\mathrm{P}}} \rho_{\mathrm{P}} \boldsymbol{\beta}_{\mathrm{P}} \cdot \boldsymbol{\eta}_{\mathrm{P}} \mathrm{d}\Gamma = \int_{\Omega_{\mathrm{F}}} g q_{\mathrm{F}} \mathrm{d}\Omega, \qquad (9)
\end{aligned}$$

for all $\left(q_{\mathrm{F}}, \mathbf{v}_{\mathrm{A}}^{\mathrm{F}}, \mathbf{v}_{\mathrm{A}}^{\mathrm{S}}, \mathbf{v}_{\mathrm{P}}, \boldsymbol{\eta}_{\mathrm{P}}\right) \in \mathbf{V}$. Here the double dot denotes the inner product for tensors, and $\boldsymbol{\epsilon}_{\mathrm{P}}$ denotes the two-dimensional strain tensor for the plate, defined in an analogous way to the tensor $\boldsymbol{\epsilon}$ in (2).

4 Finite element discretization and matrix formulation

A finite element method has been considered for computing numerically the solution of the variational problem (9), based on a quasi-uniform hexahedral mesh. With this aim, a three-dimensional hexahedral mesh, which is compatible with the boundary between the fluid and porous subdomains, has been used. The fluid pressure is discretized with continuous Q_1-Lagrange elements (one degree of freedom per vertex in Ω_{F}). Analogous $(Q_1)^3$-Lagrange elements are used to discretize the displacement fields $\mathbf{u}_{\mathrm{A}}^{\mathrm{F}}$ and $\mathbf{u}_{\mathrm{A}}^{\mathrm{S}}$ in the poroelastic subdomain, involving six degrees of freedom per vertex in Ω_{A}.

The mesh on the plate is extracted from the top faces of the porous medium mesh, resulting in a mesh composed of quadrilateral elements. The plate discretization combines standard Q_1-Lagrange elements for the membrane displacements $\mathbf{u}_{\mathrm{P}}^{\mathrm{M}}$ with MITC4 elements for the bending displacements

$\mathbf{u}_{\mathrm{P}}^3$, as shown in [31]. Elements MITC4 are the lowest order element for quadrilateral meshes within the MITC family. Bathe and Dvorkin introduced this family in [32]. It is widely used for avoiding the shear-locking phenomenon (namely, a significant reduction in numerical accuracy when the thickness of the plate decreases, which is typical for an incorrect discretization of the Reissner-Mindlin equations).

Taking into account this finite element discretization, the discrete variational problem associated with (9) in matrix form is as follows: *Find the finite element approximations $p_{\mathrm{F},h}$, $\mathbf{u}_{\mathrm{A},h}^{\mathrm{F}}$, $\mathbf{u}_{\mathrm{A},h}^{\mathrm{S}}$, $\mathbf{u}_{\mathrm{P},h}^{\mathrm{M}}$, $u_{\mathrm{P},h}^3$, and $\boldsymbol{\beta}_{\mathrm{P},h}$ which are solution of the block linear system*

$$\begin{bmatrix} \mathbf{A}_{11} & \mathbf{A}_{12} & \mathbf{A}_{13} & 0 & 0 & 0 \\ \mathbf{A}_{12}^{\mathrm{t}} & \mathbf{A}_{22} & \mathbf{A}_{23} & 0 & 0 & 0 \\ \mathbf{A}_{13}^{\mathrm{t}} & \mathbf{A}_{23}^{\mathrm{t}} & \mathbf{A}_{33} & 0 & 0 & 0 \\ 0 & 0 & 0 & \mathbf{A}_{44} & 0 & 0 \\ 0 & 0 & 0 & 0 & \mathbf{A}_{55} & \mathbf{A}_{56} \\ 0 & 0 & 0 & 0 & \mathbf{A}_{56}^{\mathrm{t}} & \mathbf{A}_{66} \end{bmatrix} \begin{bmatrix} p_{\mathrm{F},h} \\ \mathbf{u}_{\mathrm{A},h}^{\mathrm{F}} \\ \mathbf{u}_{\mathrm{A},h}^{\mathrm{S}} \\ \mathbf{u}_{\mathrm{P},h}^{\mathrm{M}} \\ u_{\mathrm{P},h}^3 \\ \boldsymbol{\beta}_{\mathrm{P},h} \end{bmatrix} = \begin{bmatrix} \mathbf{b} \\ 0 \\ 0 \\ 0 \\ 0 \\ 0 \end{bmatrix}. \tag{10}$$

Here, the first line in the left-hand side matrix stands for the integrals in Ω_{F} and its boundary,

$$\begin{aligned} q_{\mathrm{F},h}^{\mathrm{t}} \mathbf{A}_{11} p_{\mathrm{F},h} &= \frac{1}{\rho_{\mathrm{F}}\omega^2} \int_{\Omega_{\mathrm{F}}} \boldsymbol{\nabla} p_{\mathrm{F},h} \cdot \boldsymbol{\nabla} q_{\mathrm{F},h} \mathrm{d}\Omega - \frac{1}{\rho_{\mathrm{F}} c_0^2} \int_{\Omega_{\mathrm{F}}} p_{\mathrm{F},h} q_{\mathrm{F},h} \mathrm{d}\Omega, \\ q_{\mathrm{F},h}^{\mathrm{t}} \mathbf{A}_{12} \mathbf{u}_{\mathrm{A},h}^{\mathrm{F}} &= -\phi \int_{\Gamma_{\mathrm{FA}}} \mathbf{u}_{\mathrm{A},h}^{\mathrm{F}} \mathbf{n} q_{\mathrm{F},h} \mathrm{d}\Gamma, \\ q_{\mathrm{F},h}^{\mathrm{t}} \mathbf{A}_{13} \mathbf{u}_{\mathrm{A},h}^{\mathrm{S}} &= -(1-\phi) \int_{\Gamma_{\mathrm{FA}}} \mathbf{u}_{\mathrm{A},h}^{\mathrm{S}} \mathbf{n} q_{\mathrm{F},h} \mathrm{d}\Gamma. \end{aligned}$$

The second block in that matrix represents the integrals in Ω_{A},

$$\begin{aligned} (\mathbf{v}_{\mathrm{A},h}^{\mathrm{F}})^{\mathrm{t}} \mathbf{A}_{22} \mathbf{u}_{\mathrm{A},h}^{\mathrm{F}} =& R_{\mathrm{A}} \int_{\Omega_{\mathrm{A}}} \operatorname{div} \mathbf{u}_{\mathrm{A},h}^{\mathrm{F}} \operatorname{div} \mathbf{v}_{\mathrm{A},h}^{\mathrm{F}} \mathrm{d}\Omega - \omega^2 \int_{\Omega_{\mathrm{A}}} \hat{\rho}_{22} \mathbf{u}_{\mathrm{A},h}^{\mathrm{F}} \cdot \mathbf{v}_{\mathrm{A},h}^{\mathrm{F}} \mathrm{d}\Omega, \\ (\mathbf{v}_{\mathrm{A},h}^{\mathrm{F}})^{\mathrm{t}} \mathbf{A}_{23} \mathbf{u}_{\mathrm{A},h}^{\mathrm{S}} =& Q_{\mathrm{A}} \int_{\Omega_{\mathrm{A}}} \operatorname{div} \mathbf{u}_{\mathrm{A},h}^{\mathrm{S}} \operatorname{div} \mathbf{v}_{\mathrm{A},h}^{\mathrm{F}} \mathrm{d}\Omega - \omega^2 \int_{\Omega_{\mathrm{A}}} \hat{\rho}_{12} \mathbf{u}_{\mathrm{A},h}^{\mathrm{S}} \cdot \mathbf{v}_{\mathrm{A},h}^{\mathrm{F}} \mathrm{d}\Omega, \\ (\mathbf{v}_{\mathrm{A},h}^{\mathrm{S}})^{\mathrm{t}} \mathbf{A}_{33} \mathbf{u}_{\mathrm{A},h}^{\mathrm{S}} =& (P_{\mathrm{A}} - 2N_{\mathrm{A}}) \int_{\Omega_{\mathrm{A}}} \operatorname{div} \mathbf{u}_{\mathrm{A},h}^{\mathrm{S}} \operatorname{div} \mathbf{v}_{\mathrm{A},h}^{\mathrm{S}} \mathrm{d}\Omega + \int_{\Omega_{\mathrm{A}}} \boldsymbol{\epsilon}\left(\mathbf{u}_{\mathrm{A},h}^{\mathrm{S}}\right) : \boldsymbol{\epsilon}\left(\mathbf{v}_{\mathrm{A},h}^{\mathrm{S}}\right) \mathrm{d}\Omega \\ & - \omega^2 \int_{\Omega_{\mathrm{A}}} \hat{\rho}_{11} \mathbf{u}_{\mathrm{A},h}^{\mathrm{S}} \cdot \mathbf{v}_{\mathrm{A},h}^{\mathrm{S}} \mathrm{d}\Omega. \end{aligned}$$

The third block stands for the integrals on Γ_{P},

$$\begin{aligned} (\mathbf{v}_{\mathrm{P},h}^{\mathrm{M}})^{\mathrm{t}} \mathbf{A}_{44} \mathbf{u}_{\mathrm{P},h}^{\mathrm{M}} =& t \int_{\Gamma_{\mathrm{P}}} \boldsymbol{\epsilon}_{\mathrm{P}}(\mathbf{u}_{\mathrm{P},h}^{\mathrm{M}}) : \boldsymbol{\epsilon}_{\mathrm{P}}(\mathbf{v}_{\mathrm{P},h}^{\mathrm{M}}) \mathrm{d}\Gamma - \omega^2 \int_{\Gamma_{\mathrm{P}}} \rho_{\mathrm{P}} \mathbf{u}_{\mathrm{P},h}^{\mathrm{M}} \mathbf{v}_{\mathrm{P},h}^{\mathrm{M}} \mathrm{d}\Gamma, \\ (v_{\mathrm{P},h}^3)^{\mathrm{t}} \mathbf{A}_{55} u_{\mathrm{P},h}^3 =& k_{\mathrm{P}} t \int_{\Gamma_{\mathrm{P}}} \boldsymbol{\nabla} u_{\mathrm{P},h}^3 \cdot \boldsymbol{\nabla} v_{\mathrm{P},h}^3 \mathrm{d}\Gamma - \omega^2 \int_{\Gamma_{\mathrm{P}}} \rho_{\mathrm{P}} u_{\mathrm{P},h}^3 v_{\mathrm{P},h}^3 \mathrm{d}\Gamma, \\ \boldsymbol{\eta}_{\mathrm{P},h}^{\mathrm{t}} \mathbf{A}_{56} u_{\mathrm{P},h}^3 =& - k_{\mathrm{P}} t \int_{\Gamma_{\mathrm{P}}} \boldsymbol{\nabla} u_{\mathrm{P},h}^3 \cdot \mathbf{R} \boldsymbol{\eta}_{\mathrm{P},h} \mathrm{d}\Gamma, \\ \boldsymbol{\eta}_{\mathrm{P},h}^{\mathrm{t}} \mathbf{A}_{66} \boldsymbol{\beta}_{\mathrm{P},h} =& \frac{t^3}{12} \int_{\Gamma_{\mathrm{P}}} \boldsymbol{\epsilon}_{\mathrm{P}}(\boldsymbol{\beta}_{\mathrm{P},h}) \cdot \boldsymbol{\epsilon}_{\mathrm{P}}(\boldsymbol{\eta}_{\mathrm{P},h}) \mathrm{d}\Gamma + k_{\mathrm{P}} t \int_{\Gamma_{\mathrm{P}}} \mathbf{R} \boldsymbol{\beta}_{\mathrm{P},h} \cdot \mathbf{R} \boldsymbol{\eta}_{\mathrm{P},h} \mathrm{d}\Gamma \\ & - \omega^2 \frac{t^3}{12} \int_{\Gamma_{\mathrm{P}}} \rho_{\mathrm{P}} \boldsymbol{\beta}_{\mathrm{P},h} \cdot \boldsymbol{\eta}_{\mathrm{P},h} \mathrm{d}\Gamma. \end{aligned}$$

Matrices $\mathbf{A}_{56}$ and $\mathbf{A}_{66}$ involves the reduction operator $\mathbf{R}$, which is characteristic of MITC methods. In this case, the operator $\mathbf{R}$ projects the discrete functions onto the rotated Raviart-Thomas finite element space (see, for example, [33] for further details). Finally, the external source appears on the right-hand side as

$$\mathbf{b} = \int_{\Omega_{\mathrm{F}}} g q_{\mathrm{F},h} \mathrm{d}\Omega.$$

In the matrix description of the discrete coupled problem, the notation is abused since the discrete finite element functions and the complex-valued vectors with the values associated with the degrees of freedom in the finite element discretization are denoted in the same manner. Additionally, although the degrees of freedom $u^3_{\mathrm{P},h}$ and $\mathbf{u}^{\mathrm{M}}_{\mathrm{P},h}$ associated with the plate discretization and the poroelastic discretization $\mathbf{u}^{\mathrm{S}}_{\mathrm{A},h}$ seem uncoupled in the linear system (10), the coupling boundary condition (B.2) enables the assembly of the degrees of freedom of the plate displacement into the degrees of freedom associated with the poroelastic displacement of the solid part.

5 Numerical validation benchmark

The accuracy of the finite element discretization and the performance of its computer implementation have been thoroughly examined and validated using an analytical benchmark with a closed-form exact solution. To achieve this, a three-dimensional problem is stated, where the rigid boundary on the bottom is replaced by a piston-like boundary that enforces constant pressure. Specifically, the Dirichlet boundary condition $p_{\mathrm{F}}(x, y, 0) = 1$ is imposed on the fluid subdomain's bottom surface located at $z = 0$, as illustrated schematically in Figure 2.

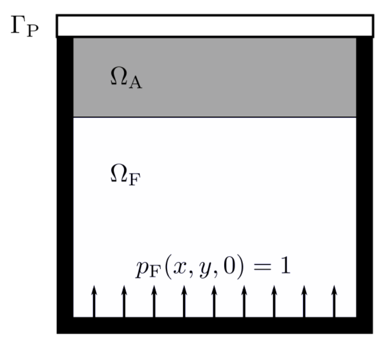

Figure 2: Two-dimensional vertical cross-section of the geometric setting used in the benchmark problem. The arrows on the bottom boundary highlight the imposed Dirichlet boundary condition on the pressure field.

If the computational domain is assumed to be a parallelepiped with all internal coupling boundaries being planar and parallel to the bottom boundary, the exact solution can be uniquely described in terms of the vertical direction due to the computational domain's symmetry. Consequently, the analytical solution can be obtained by solving a straightforward plane-wave transmission problem using the transfer matrix method (for a detailed discussion, refer to Appendix A).

The discrete variational problem (10) has been solved using successively refined uniform meshes over the parallelepiped computational domain $(-0.3, 0.3) \times (-0.3, 0.3) \times (0, 6)$ m. The poroelastic subdomain is situated between the planes $z = 0.4$ m and $z = 0.6$ m, while the elastic plate is assumed to be free and located at the top boundary $z = 0.6$. By comparing the approximated solution with the exact solution, the accuracy and convergence error of the proposed finite element discretization can be analyzed.

In the following analysis, the numerical results obtained using the finest mesh are computed for a frequency of 100 Hz. The compressible fluid is assumed to be air with properties $\rho_{\rm F} = 1.21\,{\rm kg/m^3}$ and $c_{\rm F} = 340$ m/s. The physical parameters of the poroelastic material are derived from the Acusticell material, as listed in Table 1. As for the aluminium plate in the coupled system, its properties considered include a thickness of $t = 0.001\,{\rm m}$, a Poisson ratio of $\nu_{\rm P} = 0.334$, a mass density of $\rho_{\rm P} = 2660.9\,{\rm kg/m^3}$, and complex-valued frequency-dependent Young's modulus $E_{\rm P}$, whose real and imaginary part are plotted in Figure 8(b) (see [29] for a detailed discussion).

The plots in Figures 3-5 depict the real and imaginary parts (left) as well as the L^2-relative error (right) for the pressure field in the fluid domain, the displacement field of the fluid and solid parts of the absorbing material, and the normal displacement of the plate. Since the exact solution is dependent only on the vertical direction z, all the fields are plotted at the vertices of the mesh along the central line $x = y = 0$, spanning from the midpoint of the bottom boundary to the location of the plate at the top. Specifically, for the plate displacements, the normal displacement in the z direction is plotted along the line $y = 0$, $z = 0.6$.

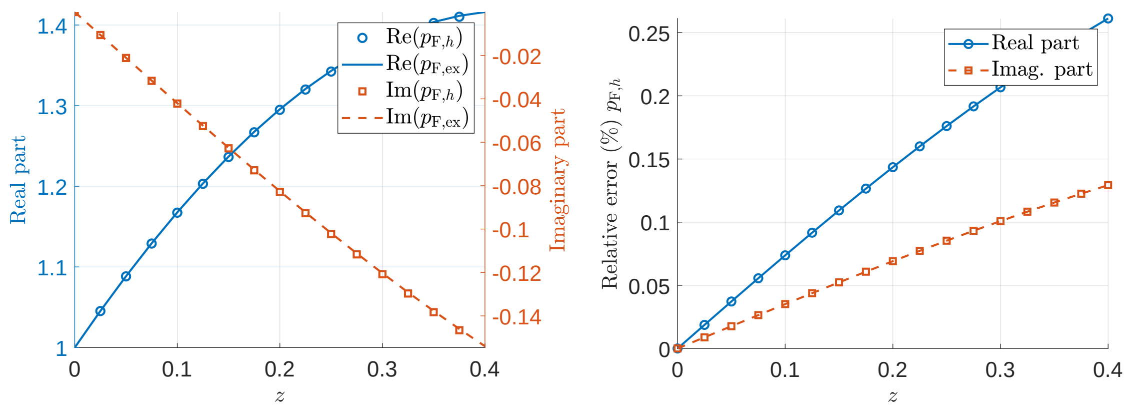

(a) Real and imaginary parts

(b) Relative error (%)

Figure 3: Numerical results of the exact and discrete approximation of the pressure field in the fluid subdomain plotted at the central line $x = y = 0$.

Figure 6 shows the L^2-relative error plotted with respect to the mesh size of the finite element discretization for the pressure field in the fluid domain and the plate displacement (left plot) and the displacement fields of the fluid and solid part of the absorbing medium (right plot). The expected second-order convergence $O(h^2)$ is observed in all cases.

6 Experimental validation

This section presents a variety of numerical simulations aimed at validating and comparing different vibroacoustic coupled models with respect to two approaches for the poroelastic material. Firstly, the numerical results obtained from the fluid-equivalent Allard-Champoux model (as conducted in [29]) are compared with the numerical results obtained using the Biot-Allard model described in this manuscript. Both sets of numerical results are validated by comparison with experimental data.

Second, the coupled problem is numerically solved again, considering both the Allard-Champoux

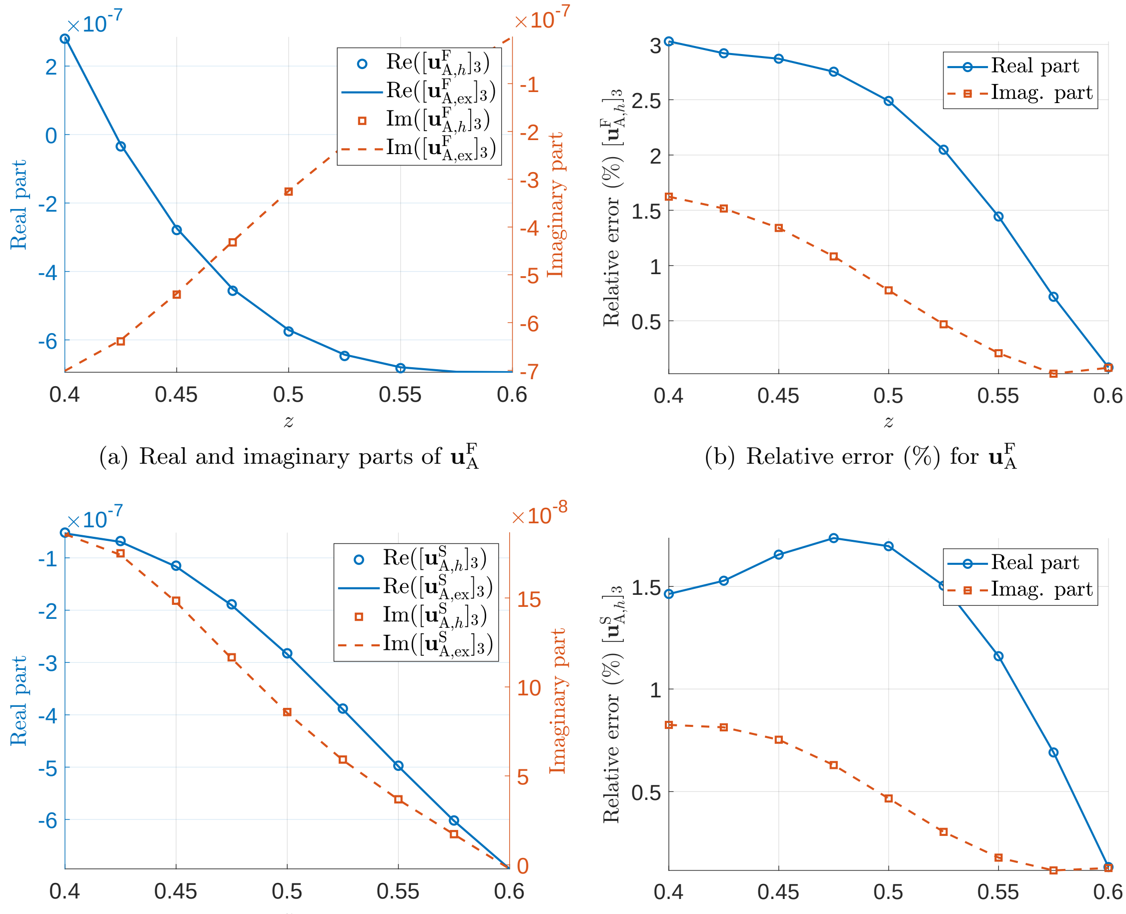

(a) Real and imaginary parts of $\mathbf{u}_{\mathrm{A}}^{\mathrm{F}}$

(b) Relative error (%) for $\mathbf{u}_{\mathrm{A}}^{\mathrm{F}}$

(c) Real and imaginary parts of $\mathbf{u}_{\mathrm{A}}^{\mathrm{S}}$

(d) Relative error (%) for $\mathbf{u}_{\mathrm{A}}^{\mathrm{S}}$

Figure 4: Numerical results of the exact and discrete approximation of the displacement fields $\mathbf{u}_{\mathrm{A}}^{\mathrm{F}}$ and $\mathbf{u}_{\mathrm{A}}^{\mathrm{S}}$ in the poroelastic subdomain plotted at the central line $x = y = 0$.

and the Biot-Allard models, but now in two distinct scenarios. These scenarios involve placing the acoustic source in frontal and lateral configurations within the fluid cavity. By examining the plate vibrations in these two scenarios, qualitatively different behaviours between the two models are observed.

6.1 Experimental setting

The same experimental setup described in [29] has been employed for the experimental validation in this study. It is important to note that quasi-uniform hexahedral and quadrilateral meshes were utilized for the Allard-Champoux and Biot-Allard simulations, although with slight variations in each case. In the numerical tests presented in [29], non-matched meshes were used, with an element size of 0.02 m for the plate and 0.1 m for the fluid domain. However, for the numerical results corresponding to the Biot-Allard model, refined compatible meshes with an element size of 0.025 m have been employed for all subdomains (fluid, poroelastic, and plate).

The experimental validation setup (see Figure 7) comprises a 0.6 m × 0.6 m × 0.6 m parallelepiped box. Five of its faces are rigid, made of wood with a thickness of 0.040 m and covered with an

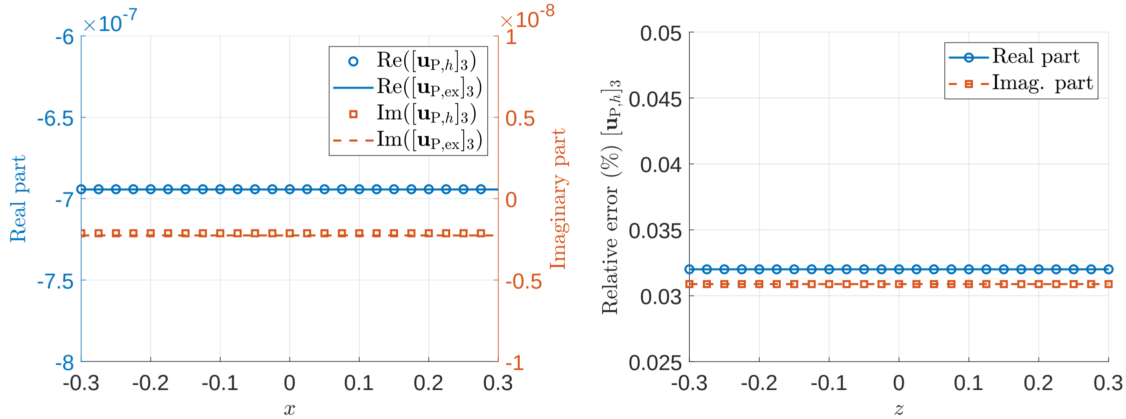

(a) Real and imaginary parts

(b) Relative error (%)

Figure 5: Numerical results of the exact and discrete approximation of the normal displacement field on the plate plotted at the line $y = 0,\ z = 0.6$.

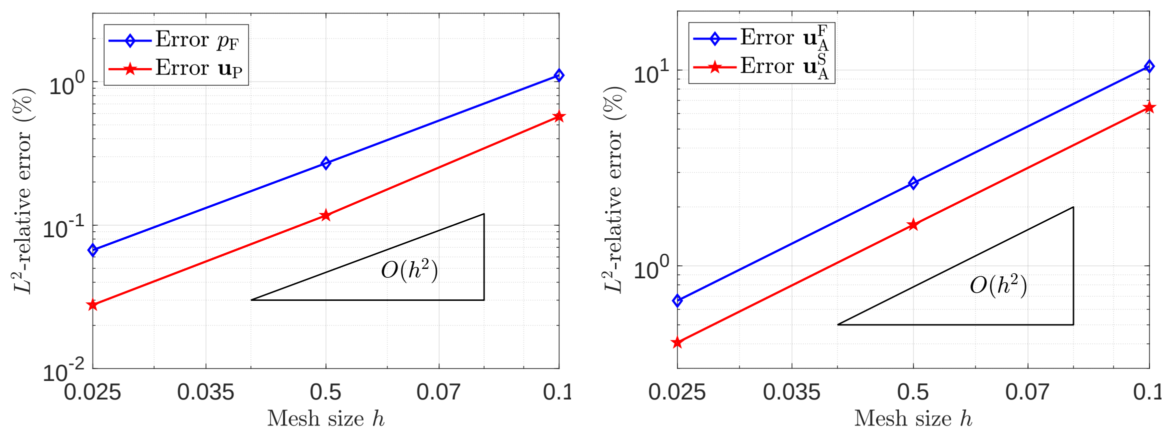

Figure 6: Convergence curves for the finite element approximation of the fluid pressure field and the displacements in the poroelastic subdomain and the plate.

aluminium layer. The top face consists of a flexible aluminium plate with a thickness of 0.001 m. The plate is rigidly joined to the remaining walls of the cavity using screws.

A calibrated loudspeaker serves as the acoustic source, positioned at the centre of the base and considered as a baffled source. In the numerical model, the loudspeaker is represented as a pulsating sphere, and the source term in (1) is modelled as a monopole $g = i\hat{Q}/\omega\delta_{\mathrm{x}_0}$, where δ_{x_0} denotes the Dirac's delta function supported at $x_0 \in \Omega_{\mathrm{F}}$. The volume velocity of the loudspeaker, denoted as $\hat{Q}$, has been experimentally determined using the method proposed in [34]. A comprehensive description of the source characterization is provided in [29], and the frequency response of $\hat{Q}$ is illustrated in Figure 8(a).

Once the cavity is excited by the loudspeaker with a random signal in the frequency range of interest, the acoustic pressure is measured experimentally at nine different points inside the cavity (see the black points sketched in Figure 8(c)) being normalized by the loudspeaker input voltage at each point (see Figure 8(d)). The root mean squared (RMS) value is obtained from the amplitude of

(a) Exterior

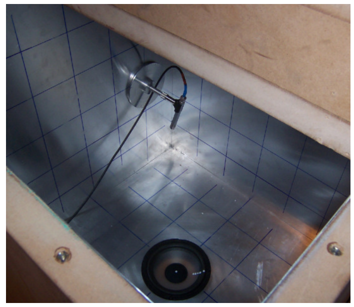

(b) Interior

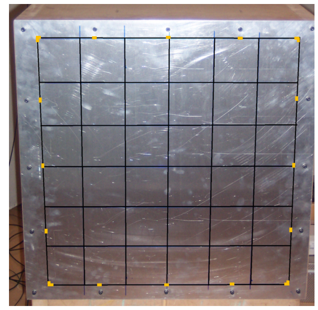

(c) Plate

Figure 7: Experimental validation setting with a detailed view of the exterior, interior (with the frontal location of the loudspeaker in the bottom), and the plate (where the screw locations are highlighted in yellow).

those measurements, that is, RMS $= \sqrt{\sum_{j=1}^{9} |p_{\mathrm{F}}(\mathbf{x}_j)/V(\mathbf{x}_j)|^2}$, where recall p_{F} is the fluid pressure, V is the loudspeaker input voltage measured experimentally, and $\mathbf{x}_j$ are the spatial coordinates of the measurement points depicted in Figure 8(c).

As in [29], the plate has been assumed clamped in the locations of the screws (see the plate boundary highlighted in yellow in Figure 7(c)). Additionally, the plate Young's modulus has been characterized experimentally according to the ASTM754-04 standard [35] measuring its real and imaginary part by the method proposed by Caraccilo *et al.* in [36].

Regarding the physical values taken into account in the experimental validation, the mass density of the fluid (air at normal conditions) is assumed $\rho_{\mathrm{F}} = 1.21\ \mathrm{kg/m^3}$ and its speed of sound $c_{\mathrm{F}} = 340\ \mathrm{m/s}$. The physical values for the two absorbent materials are listed in Table 1. Finally, the mechanical behaviour of the aluminium plate is characterized by its mass density $\rho_{\mathrm{P}} = 2660.9\ \mathrm{kg/m^3}$, the Poisson's coefficient $\nu_{\mathrm{P}} = 0.334$, and the complex-valued Young's modulus whose frequency response functions for the real and imaginary parts are plotted in Figure 8(b).

Porous layer	Acustifiber P	Acusticell
Thickness (10^{-3} m):	39	24
Flow resistivity, r : ($\mathrm{Ns/m^4}$)	2000	22000
Porosity, ϕ:	>0.95	>0.95
Tortuosity, α_∞:	1.03	1.38
Viscous length, Λ (10^{-6}m):	420	17
Thermal length, Λ' (10^{-6}m):	650	40
Skeleton density, ρ_{S}($\mathrm{kg/m^3}$):	17	26
Young Modulus, E_{A}(kPa):	13	192
Loss factor, η_{A}:	0.23	0.13
Poisson ratio, ν_{A}:	0.0	0.23

Table 1: Physical parameters of the Biot-Allard model for Acoustifiber P and Acusticell absorbing materials.

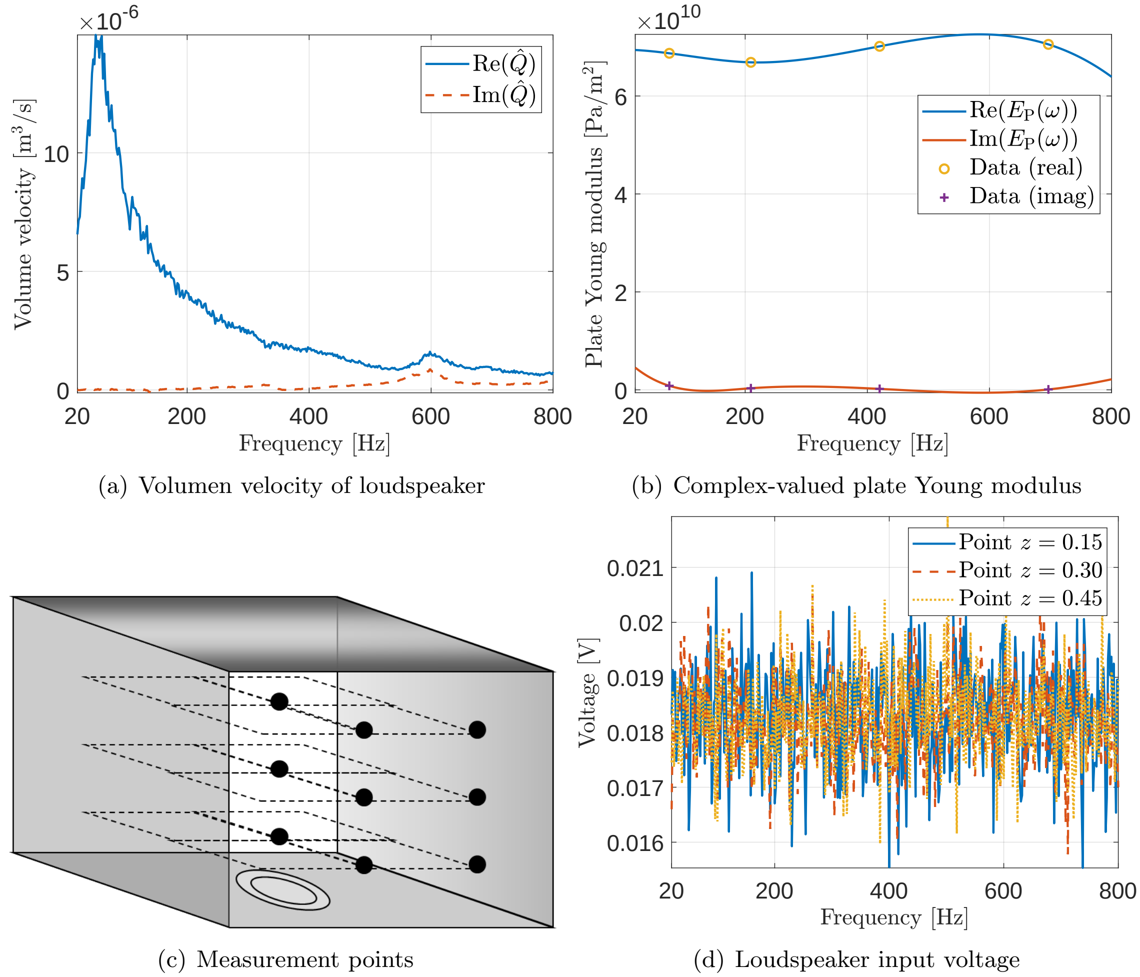

(a) Volumen velocity of loudspeaker

(b) Complex-valued plate Young modulus

(c) Measurement points

(d) Loudspeaker input voltage

Figure 8: Frequency response function of loudspeaker volume velocity (top-left) and complex-valued Young modulus of the plate (top-right). Location of measurement points (bottom-left) and input voltage (bottom-right).

6.2 Scenario with a frontal acoustic source

First, an acoustic excitation is positioned in front of the plate and the absorbing layer, located at the centre of the base of the fluid cavity ($x_0 = (x, y, z) = (0.30, 0.30, 0.00)$). Figure 9 shows the RMS frequency response function for both absorbent materials detailed in Table 1, comparing the experimental data, the numerical results obtained using the Allard-Champoux fluid-equivalent model (as described in [29]), and the results obtained using the Biot-Allard model described in this work. In this figure, it can be observed that both numerical methods provide accurate approximations of the resonance frequencies of the coupled system. However, the model presented in this study (blue curve) exhibits superior predictive capabilities throughout the entire frequency spectrum, closely matching the experimental response observed in the laboratory.

Figures 10 and 11 show the numerical results obtained from both methods for two resonance frequencies: 70 Hz (second mode of the coupled system) and 286 Hz (third mode of the coupled system, which is closed to the first mode of the fluid cavity). For both methods, the pressure magnitude in the fluid and the normal displacement magnitude in the plate are displayed. With

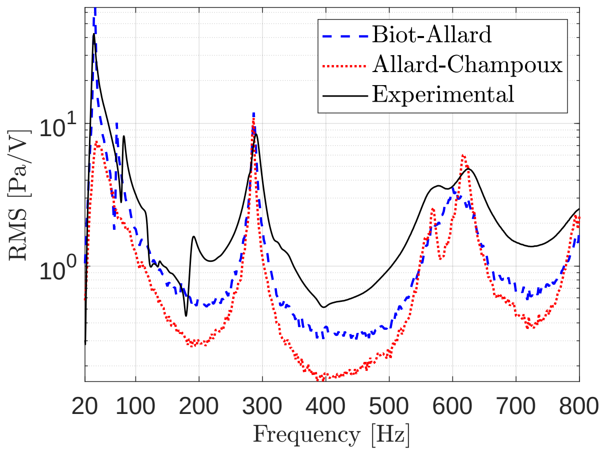

(a) Acusticel absorbing material

(b) Acustifiber absorbing material

Figure 9: Comparison of the experimental data with the finite element approximation of the RMS frequency response in a frontal source scenario.

respect to the porous medium, due to the use of a different discretization variable, the pressure field is shown for the Allard-Champoux model and the vertical component of the displacement of the solid part for the Biot-Allard model.

6.3 Scenario with a lateral acoustic source

The second test-case scenario involves a lateral excitation, where the same acoustic source is positioned at the centre of one of the side walls of the fluid cavity ($\mathbf{x}_0 = (x, y, z) = (0.00, 0.30, 0.30)$). Figure 12 presents the RMS frequency response for both the Allard-Champoux and Biot-Allard models. While this lateral configuration has not been experimentally reproduced, the available experimental data from the frontal configuration has been included in the figure as a reference curve.

Similar to frontal excitation, the model presented in this study demonstrates enhanced predictive ability within the analysed frequency range. By incorporating two compression waves and one shear wave in the porous medium, the Biot-Allard model combined with Nagdhi's plate formulation accurately captures the plate's dynamic behaviour. Consequently, it produces more precise results compared to the Allard-Champoux model.

Figure 13 shows the pressure and displacement fields computed using both models at a frequency of 286 Hz, corresponding to the excitation of the first resonance mode in the fluid cavity. The same fields as those shown in Figures 10 and 11 are displayed, including fluid pressures and normal displacements in the plate. In the case of the poroelastic layer, the pressure field is plotted for the Allard-Champoux model, while vertical displacements are depicted for the Biot-Allard model.

Figure 14 presents the in-plane displacements on the plate for this lateral source scenario. Specifically, the displacements in the x and y directions are plotted on the left and right-hand panels, respectively. It can be observed that these displacements are several orders of magnitude smaller than the normal displacements. However, accurately capturing these displacements can be advantageous in certain practical applications, such as when multiple folded plates cover the fluid. The proposed coupled modelling approach using the Biot-Allard governing equations in this study successfully achieves this objective. In contrast, the Allard-Champoux model does not account for these displacements due to its fluid-equivalent modelling approach.

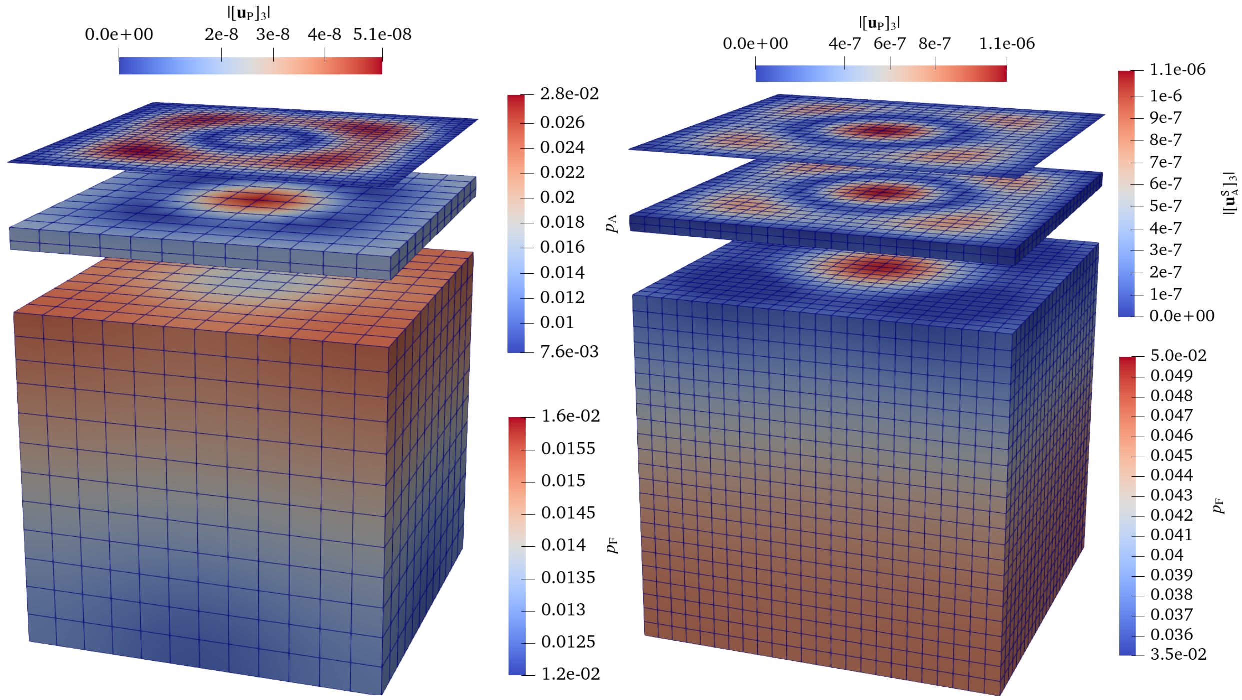

Figure 10: Finite element approximation of the fluid pressure field and the vertical displacements for the Allard-Champoux model (left) and the Biot-Allard model (right) at 70 Hz in the frontal source scenario. The geometry has been exploited and translated to better inspect the fields at the coupling boundaries.

7 Conclusions

A detailed description of a coupled vibroacoustic problem has been provided, involving a compressible fluid domain and an elastic plate coated with a poroelastic layer. The acoustic fluid is modelled based on the pressure field, whereas the poroelastic material is governed by the Biot-Allard model written in a displacement-based formulation. Additionally, the fluid-equivalent Allard-Champoux model, which only considers the pressure field, has also been considered for comparison purposes. The plate vibrations are modelled using the Naghdi plate model, accounting for the in-plane and the normal displacements of the middle layer of the plate and the rotations of the initially normal fibres. The coupled vibroacoustic system is discretized using bilinear Lagrange elements for the fluid and poroelastic medium on hexahedral meshes and mixed MITC4 elements for the elastic plate.

The finite element implementation has been validated on a test example with a known closed-form solution, demonstrating optimal convergence order. Subsequently, the frequency response using both the Allard-Champoux and Biot-Allard models has been numerically computed and compared with experimental data in two test-case scenarios: frontal and lateral locations for the acoustic source. The Biot-Allard approach accurately predicts the experimental results when a frontal excitation is considered, surpassing the numerical results obtained by the equivalent fluid Allard-Champoux model. In the case of a lateral excitation where the acoustic source is placed with respect to the poroelastic layer, the advantages of using the Biot-type model are evident. It allows for the prediction of not only the normal displacements of the elastic plate but also the membrane (in-plane) displacements, which are neglected in the Allard-Champoux model. This vibroacoustic

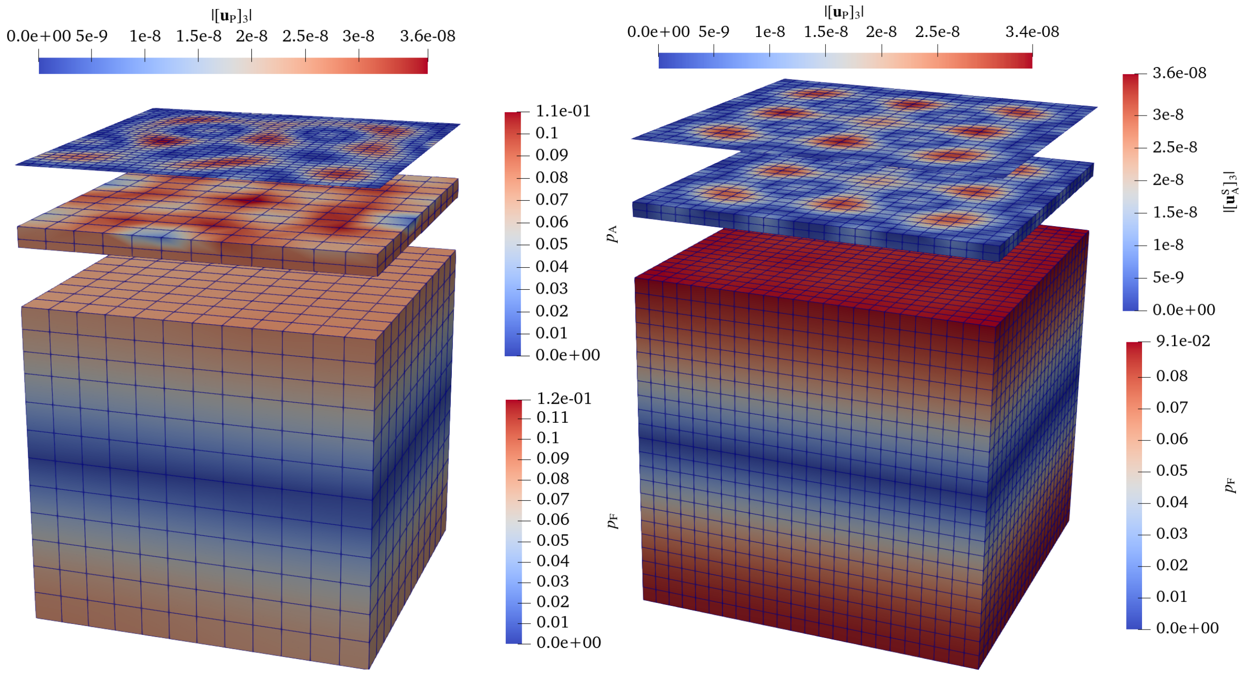

Figure 11: Finite element approximation of the fluid pressure field and the vertical displacements for the Allard-Champoux model (left) and the Biot-Allard model (right) at 286 Hz in the frontal source scenario. The geometry has been exploited and translated to better inspect the fields at the coupling boundaries.

feature is crucial in industrial applications where shear stresses need to be predicted on structures where the poroelastic patches are located.

A Plane-wave solution of a piston-like benchmark

A plane wave solution under normal incidence is sought across the fluid and poroelastic domains to obtain the analytical expression of the exact solution in the benchmark test (see Section 5). Considering the symmetry of the boundary conditions and the computational domain, the solution depends only on the z-coordinate. Hence, it can be written as a linear combination of compressional plane waves. Specifically, the pressure field, as well as the vertical component of the fluid and solid displacement fields in the absorbing subdomain, can be expressed as follows:

$$p_\mathrm{F}(z) = P_\mathrm{F}^\mathrm{i} e^{-ik_\mathrm{F} z} + P_\mathrm{F}^\mathrm{r} e^{+ik_\mathrm{F} z},$$
$$u_\mathrm{A}^\mathrm{S3}(z) = e^{-ik_\mathrm{A}^+ z} U_\mathrm{A}^\mathrm{S,1i} + e^{+ik_\mathrm{A}^+ z} U_\mathrm{A}^\mathrm{S,1r} + e^{-ik_\mathrm{A}^- z} U_\mathrm{A}^\mathrm{S,2i} + e^{+ik_\mathrm{A}^- z} U_\mathrm{A}^\mathrm{S,2r}, \quad u_\mathrm{A}^\mathrm{F3}(z) = \mu_\mathrm{A} u_\mathrm{A}^\mathrm{S3}(z),$$

where the fluid and poroelastic compressional wavenumber are $k_\mathrm{F} = \omega/c_\mathrm{F}$ and

$$k_\mathrm{A}^\pm = \omega \sqrt{\frac{b + \sqrt{b^2 - 4a(\hat{\rho}_{11}\hat{\rho}_{22} - \hat{\rho}_{12}^2)}}{2a}},$$

being $b = R_\mathrm{A}\hat{\rho}_{11} + P_\mathrm{A}\hat{\rho}_{22} - 2Q_\mathrm{A}\hat{\rho}_{12}$ and $a = R_\mathrm{A} P_\mathrm{A} - Q_\mathrm{A}^2$ (see [9] for further details). The amplitude ratio μ_A between the amplitude of the displacements of fluid and solid parts in the absorbing medium is given by $\mu_\mathrm{A} = (P_\mathrm{A}(k_\mathrm{A}^\pm)^2 - \omega^2\hat{\rho}_{11})/(\omega^2\hat{\rho}_{12} - Q_\mathrm{A}(k_\mathrm{A}^\pm)^2)$.

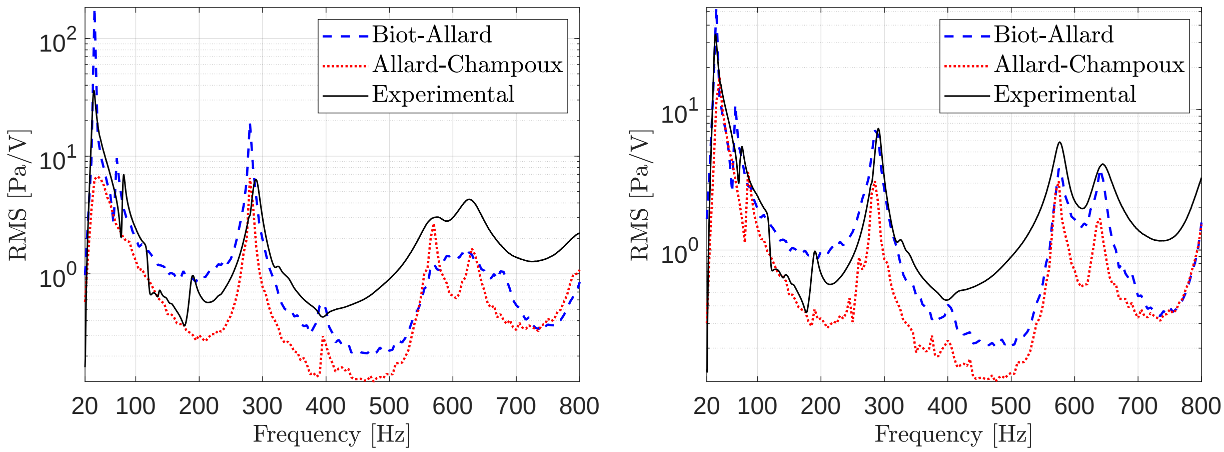

(a) Acusticel absorbing material

(b) Acustifiber absorbing material

Figure 12: Comparison of the experimental data with the finite element approximation of the RMS frequency response in a lateral source scenario.

Since the pressure and displacement fields in the poroelastic subdomains only depend on the z-coordinate, the loads exerted by the absorbing material on the plate at $z = 0.6$ will be constant. Hence, combining this fact with the simply supported boundary conditions imposed on the plate leads to $\boldsymbol{\beta} = (\beta_1, \beta_2) = (0, 0)$, and the normal displacement on the plate will be constant. Consequently, the governing equation of the plate is reduced to $t\rho_{\mathrm{P}}\omega^2 u_{\mathrm{P}}^3 = g_{\mathrm{P}}$.

Now, applying the coupling boundary conditions (A)-(D) and the boundary condition associated with the Dirichlet boundary condition on the bottom boundary leads to the following linear system of equations:

$$P_{\mathrm{F}}^{\mathrm{i}} + P_{\mathrm{F}}^{\mathrm{r}} = 1,$$

$$\begin{aligned}
&e^{-ik_{\mathrm{F}}(H-t_{\mathrm{A}})}P_{\mathrm{F}}^{\mathrm{i}} + e^{+ik_{\mathrm{F}}(H-t_{\mathrm{A}})}P_{\mathrm{F}}^{\mathrm{r}} \\
&\qquad + ik_1\left[P_{\mathrm{A}} + Q_{\mathrm{A}}(\mu_1+1) + R_{\mathrm{A}}\mu_1\right]\left(-e^{-ik_1(H-t_{\mathrm{A}})}U_{\mathrm{A}}^{\mathrm{S,1i}} + e^{ik_1(H-t_{\mathrm{A}})}U_{\mathrm{A}}^{\mathrm{S,1r}}\right) \\
&\qquad\qquad + ik_2\left[P_{\mathrm{A}} + Q_{\mathrm{A}}(\mu_2+1) + R_{\mathrm{A}}\mu_2\right]\left(-e^{-ik_2(H-t_{\mathrm{A}})}U_{\mathrm{A}}^{\mathrm{S,2i}} + e^{ik_2(H-t_{\mathrm{A}})}U_{\mathrm{A}}^{\mathrm{S,2r}}\right) = 0,
\end{aligned}$$

$$\begin{aligned}
&\frac{ik_{\mathrm{F}}}{\rho_{\mathrm{F}}\omega^2}\left(-e^{-ik_{\mathrm{F}}(H-t_{\mathrm{A}})}P_{\mathrm{F}}^{\mathrm{i}} + e^{+ik_{\mathrm{F}}(H-t_{\mathrm{A}})}P_{\mathrm{F}}^{\mathrm{r}}\right) \\
&\qquad - \left[1 + \phi(\mu_1 - 1)\right]\left(e^{-ik_1(H-t_{\mathrm{A}})}U_{\mathrm{A}}^{\mathrm{S,1i}} + e^{ik_1(H-t_{\mathrm{A}})}U_{\mathrm{A}}^{\mathrm{S,1r}}\right) \\
&\qquad\qquad - \left[1 + \phi(\mu_2 - 1)\right]\left(e^{-ik_2(H-t_{\mathrm{A}})}U_{\mathrm{A}}^{\mathrm{S,2i}} + e^{ik_2(H-t_{\mathrm{A}})}U_{\mathrm{A}}^{\mathrm{S,2r}}\right) = 0,
\end{aligned}$$

$$\begin{aligned}
&e^{-ik_{\mathrm{F}}(H-t_{\mathrm{A}})}P_{\mathrm{F}}^{\mathrm{i}} + e^{+ik_{\mathrm{F}}(H-t_{\mathrm{A}})}P_{\mathrm{F}}^{\mathrm{r}} \\
&\qquad + \frac{ik_1}{\phi}(Q_{\mathrm{A}} + R_{\mathrm{A}}\mu_1)\left(-e^{-ik_1(H-t_{\mathrm{A}})}U_{\mathrm{A}}^{\mathrm{S,1i}} + e^{ik_1(H-t_{\mathrm{A}})}U_{\mathrm{A}}^{\mathrm{S,1r}}\right) \\
&\qquad\qquad + \frac{ik_2}{\phi}(Q_{\mathrm{A}} + R_{\mathrm{A}}\mu_2)\left(-e^{-ik_2(H-t_{\mathrm{A}})}U_{\mathrm{A}}^{\mathrm{S,2i}} + e^{ik_2(H-t_{\mathrm{A}})}U_{\mathrm{A}}^{\mathrm{S,2r}}\right) = 0,
\end{aligned}$$

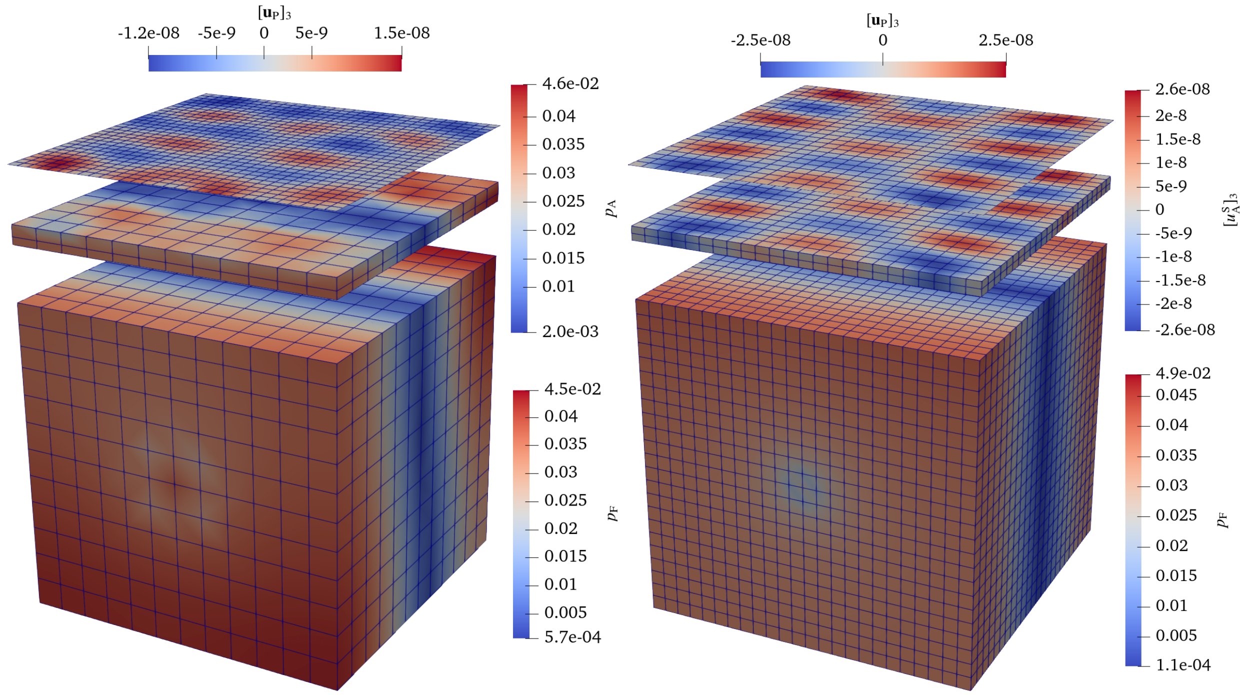

Figure 13: Finite element approximation of the fluid pressure field and the vertical displacements for the Allard-Champoux model (left) and the Biot-Allard model (right) at 286 Hz in the lateral source scenario. The geometry has been exploited and translated to better inspect the fields at the coupling boundaries.

$$
\begin{gathered}
e^{-ik_1H}U_{\mathrm{A}}^{\mathrm{S,1i}} + e^{ik_1H}U_{\mathrm{A}}^{\mathrm{S,1r}} + e^{-ik_2H}U_{\mathrm{A}}^{\mathrm{S,2i}} + e^{ik_2H}U_{\mathrm{A}}^{\mathrm{S,2r}} - u_{\mathrm{P}}^3 = 0,\\
(\mu_1 - 1)\left(e^{-ik_1H}U_{\mathrm{A}}^{\mathrm{S,1i}} + e^{ik_1H}U_{\mathrm{A}}^{\mathrm{S,1r}}\right) + (\mu_2 - 1)\left(e^{-ik_2H}U_{\mathrm{A}}^{\mathrm{S,2i}} + e^{ik_2H}U_{\mathrm{A}}^{\mathrm{S,2r}}\right) = 0,
\end{gathered}
$$

$$
\begin{aligned}
ik_1\left[P_{\mathrm{A}} + Q_{\mathrm{A}}(\mu_1+1) + R_{\mathrm{A}}\mu_1\right]&\left(-e^{-ik_1H}U_{\mathrm{A}}^{\mathrm{S,1i}} + e^{ik_1H}U_{\mathrm{A}}^{\mathrm{S,1r}}\right)\\
&+ ik_2\left[P_{\mathrm{A}} + Q_{\mathrm{A}}(\mu_2+1) + R\mu_2\right]\left(-e^{-ik_2H}U_{\mathrm{A}}^{\mathrm{S,2i}} + e^{ik_2H}U_{\mathrm{A}}^{\mathrm{S,2r}}\right) - t\rho_{\mathrm{P}}\omega^2 u_{\mathrm{P}}^3 = 0,
\end{aligned}
$$

where H is the height of the parallepiped computational domain and t_{A} is the thickness of the porous layer.

References

[1] A.K. Kan, X.X. Zhang, Z.F. Chen, and D. Cao. Effective thermal conductivity of vacuum insulation panels prepared with recyclable fibrous cotton core. *International Journal of Thermal Sciences*, 187(108176), 2023.

[2] M.A. Heckl. Analytical model of nonlinear thermo-acoustic effects in a matrix burner. *J. Sound Vib.*, 332:4021–4036, 2013.

[3] N. Curry, M. Letner, and K. Körner. Recent developments of thermal barrier coatings. *Open Access Article*, 2020.

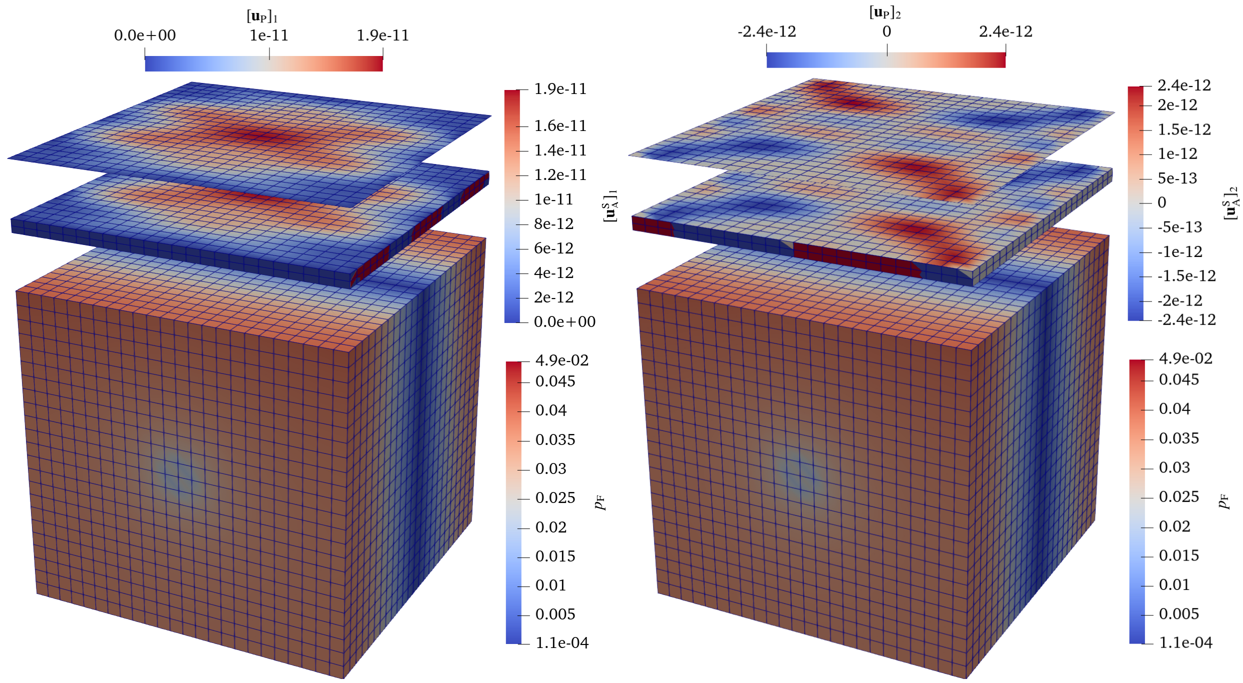

Figure 14: Finite element approximation of the fluid pressure field and the in-plane displacements for the Biot-Allard model at 286 Hz in the lateral source scenario (x-axis component on the right and y-axis component on the left). The geometry has been exploited and translated to better inspect the fields at the coupling boundaries.

[4] Y. Liu and A. Sebastian. Effects of external and gap mean flows on sound transmission through a double-wall sandwich panel. *J. Sound Vib.*, 344:399–415, 2015.

[5] P. Soltani and M. Norouzi. Prediction of the sound absorption behavior of nonwoven fabrics: Computational study and experimental validation. *J. Sound Vib.*, 485(115607), 2020.

[6] D. Barpanda and J. M. Tudor. Solutions-based approach for reducing noise in washing machines. *Sound and Vibration*, 43(11):6–10, 2009.

[7] A. Takezawa, T. Yamamoto, X. Zhang, K. Yamakawa, S. Nakano, and M. Kitamura. An objective function for the topology optimization of sound-absorbing materials. *J. Sound Vib.*, 443:804–819, 2019.

[8] E. Taban and al. Measurement, modeling, and optimization of sound absorption performance of kenaf fibers for building applications. *Building and Environment*, 180(107087), 2020.

[9] J.F. Allard and N. Atalla. *Propagation of Sound in Porous Media: Modelling Sound Absorbing Materials*. John Wiley & Sons, 2009.

[10] X. Sagartzazu, L. Hervella-Nieto, and J. M. Pagalday. Review in sound absorbing material. *Arch. Comput. Meth. Engng.*, 15:311–342, 2008.

[11] I.I. Beranek and I.L. Vér. *Noise and Vibration Control Engineering: Principles and Applications*. Wiley-Interscience, 1992.

[12] A. Bermúdez, L. M. Hervella-Nieto, and R. Rodríguez. Finite element computation of the vibration of a plate-fluid system with interface damping. *Comput*, 190:3021–3038, 2001.

[13] A. Bermúdez, J. L. Ferrín, and A. Prieto. A finite element solution of acoustic propagation in rigid porous media. *International Journal for Numerical Methods in Engineering*, 62(10):1295–1314, 2005.

[14] D. L. Johnson, J. Koplik, and R. Dashen. Theory of dynamic permeability and tortuosity in fluid-saturated porous media. *J. Fluid Mechanics*, 176:379–402, 1987.

[15] J. F. Allard and Y. Champoux. New empirical equations for sound propagation in rigid frame fibrous materials. *J. Acoust. Soc. Am.*, 91:3346–3353, 1992.

[16] P. Göransson. A weighted residual formulation of the acoustic wave propagation through a flexible porous material and comparison with a limp material model. *J. Sound Vib.*, 182:479–494, 1995.

[17] R. Panneton and N. Atalla. Numerical prediction of sound transmission through finite multilayer systems with poroelastic materials. *J. Acoust. Soc. Am.*, 100(1):346–354, 1996.

[18] R. Panneton and N. Atalla. An efficient finite element scheme for solving the three dimensional poroelasticity problem in acoustics. *J. Acoust. Soc. Am.*, 101(6):3287–3298, 1997.

[19] M.A. Biot. The theory of propagation of elastic waves in a fluid saturated porous solid. *J. Acoust. Soc. Am*, 28:168–178, 1956.

[20] T. Bravo and C. Maury. Sound attenuation and absorption by anisotropic fibrous materials: Theoretical and experimental study. *J. Sound Vib.*, 417:165–181, 2018.

[21] T. G. Zieliński, R. Venegas, C. Perrot, M. Červenka, F. Chevillotte, and K. Attenborough. Benchmarks for microstructure-based modelling of sound absorbing rigid-frame porous media. *J. Sound Vib.*, 483(115441), 2020.

[22] A. Bermudez, J. L. Ferrín, and A. Prieto. Finite element solution of new displacement/pressure poroelastic models in acoustics. *Computer Methods in Applied Mechanics and Engineering*, 195(17-18):1914–1932, 2006.

[23] G. Ciaburro and G. Iannace. Modeling acoustic metamaterials based on reused buttons using data fitting with neural network. *J. Acoust. Soc. Am.*, 150(1):51–63, 2021.

[24] N. Atalla, R. Panneton, and P. Debergue. A mixed displacement-pressure formulation for poroelastic materials. *J. Acoust. Soc. Am.*, 104(3):1444–1452, 1998.

[25] N. Atalla and R. Panneton. Acoustic absorption of macro-perforated porous materials. *J. Sound and Vibration*, 243:659–678, 2001.

[26] A. Bermúdez, P. Gamallo, L. Hervella-Nieto, R. Rodríguez, and D. Santamarina. Fluid-structure acoustic interaction. In S. Marburg and B. Nolte, editors, *Computational Acoustics of Noise Propagation in Fluids*, pages 253–286. Springer-Verlag, 2008.

[27] P. M. Naghdi. The theory of shells and plates. In C. Truesdell, editor, *Linear Theories of Elasticity and Thermoelasticity: Linear and Nonlinear Theories of Rods, Plates, and Shells*, pages 425–640. Springer Berlin Heidelberg, Berlin, Heidelberg, 1973.

[28] D.N. Arnold and R.S. Falk. Asymptotic analysis of the boundary layer for the reissner-mindlin plate model. *SIAM Journal on Mathematical Analysis*, 27(2):486–514, 1996.

[29] X. Sagartzazu, L. Hervella-Nieto, and J. M. Pagalday. Numerical computation of the acoustic pressure in a coupled covered plate/fluid problem: Experimental validation. *Acta Acustica united with Acustica*, 96:317–327, 2010.

[30] A. Bermúdez, P. Gamallo, L. Hervella-Nieto, and R. Rodríguez. Finite element analysis of pressure formulation of the elastoacoustic problem. *Numer. Math.*, 95:29–51, 2003.

[31] E. Hernández and L. Hervella-Nieto. Finite element approximation of free vibration of folded plates. *Comput. Methods Appl. Mech. Engng.*, 198:1360–1367, 2009.

[32] K.J. Bathe and E.N. Dvorkin. A four-node plate bending element based on mindlind/reissner plate theory and a mixed interpolation. *Int. J. Numer. Meth. Engng*, 21:367–383, 1985.

[33] R.G. Durán, E. Hernández, L. Hervella-Nieto, E. Liberman, and R. Rodríguez. Error estimates for low-order isoparametric quadrilateral finite elements for plates. *SIAM J. Numer. Anal.*, 41:1751–1772, 2003.

[34] D.K. Anthony and S.J. Elliot. A comparison of three methods of measuring the volume velocity of an acoustic source. *J. Audio Eng. Soc.*, 39:355–365, 1991.

[35] ASTM E756-04. *Standard test method for measuring vibration-damping properties of materials.* American Society for Testing and Materials, 2004.

[36] R. Caracciolo, A. Gasparetto, and M. Giovagnoni. An experimental technique for complete dynamic characterization of a viscoelastic material. *J. Sound Vib.*, 272:1013–1032, 2004.